Journal of Nuclear Materials 378 (2008) 144–152

Contents lists available at ScienceDirect

Journal of Nuclear Materials

journal homepage: www.elsevier.com/locate/jnucmat

Oxidation and creep failure of alloy 617 foils at high temperature

S.K. Sharma, G.D. Ko, F.X. Li, K.J. Kang *

Department of Mechanical Engineering, Chonnam National University, Gwangju 500 757, Republic of Korea

ARTICLE INFO

Article history:
Received 3 September 2007
Accepted 30 April 2008

PACS:
68.49.−h
68.37.−d
62.20.Hg
61.72.Mn

ABSTRACT

The microstructure of thermally grown oxides (TGO) and the creep properties of alloy 617 were investigated. Oxidation and creep tests were performed on 100 μm thick foils at 800–1000 °C in air environment, while the thickness of TGO was monitored *in situ*. According to energy dispersive X-ray (EDX) mapping micrographs observation, superficial dense oxides, chromia (Cr_2O_3), which was thermodynamically unstable at 1000 °C, and discrete internal oxides, alumina (α-Al_2O_3), were found. Consequently, the weight of the foil specimen decreased due to the spalling and volatilization of the Cr_2O_3 oxide layer after an initial weight-gaining. Secondary and tertiary creeps were observed at 800 °C, while the primary, secondary and tertiary creeps were observed at 1000 °C. Dynamic recrystallization occurred at 800 °C and 900 °C, while partial dynamic recrystallization at 1000 °C. The apparent activation energy, Q_{app}, for the creep deformation was 271 kJ/mol, which was independent of the applied stress.

1. Introduction

Very high temperature gas-cooled reactor (VHTR) designs aim for hydrogen production and electric power generation. Ni-base alloys are the candidate materials for VHTR due to their excellent material properties, namely, oxidation resistance, creep strength, and phase stability, at high temperatures. Alloy 617 has been selected as a potential candidate for use in the construction of the internal components, piping, and heat exchangers of the VHTR [1,2]. Alloy 617 is an austenitic solid-solution strengthened, Ni-base alloy, which contains chromium (Cr), cobalt (Co), molybdenum (Mo) and aluminum (Al). Al and Cr contents protect the alloy from oxidation reaction at high temperatures. Mo and Co provide solid solution strengthening, and $M_{23}C_6$ carbides provide strength through precipitation hardening [1,3–8]. This solution is normally used in the annealed condition, which provides a coarse grain structure to realize the best creep rupture strength [9–10].

The predicted service temperature of VHTR can reach 1000 °C or higher. At this temperature, the oxidation behavior of alloy 617 becomes one of the major life-limiting factors. Thermally grown oxide (TGO) is usually formed on the surface of the alloy when the alloy is exposed to high temperature in air and moisture containing inert gaseous environment. The TGO might play an important role in enhancement of the creep strength; that is, it increases the resistance to creep failure at elevated temperatures [11]. Therefore, it is necessary to investigate the oxidation behavior of the alloy in an air environment. Christ et al. [12] have shown that a compact layer of Cr_2O_3 was formed on the surface of alloy 617 at 950 °C. They also reported that the kinetics of its oxidation was determined by the transport of CO_2 and H_2O in an inert gas.

Alloys are subject to degradation due to creep when they are exposed to VHTR for a prolonged period. Therefore, the creep properties of candidate alloys should be well understood and thoroughly characterized before the alloys are used in the design and construction of internal components of VHTR. The creep rupture lives are known to be strongly dependent on the alloy's microstructure as well as the test temperature and the applied stresses. Extensive creep studies have indicated that the creep rate of a metal is proportional to both the diffusion coefficient and the power of the applied stress [13]. The effects of recrystallization and grain boundary migration on the creep strength of alloy 617 at 1100 °C were studied. Partial recrystallization was observed during a creep test after the alloy was annealed at 1000 °C [6].

With respect to VHTR application, Shankar et al. [10] have investigated the environmental effect on the creep fracture characteristic of alloy 617 at high temperatures. Creep fracture in pure He and He + O_2 environments occurred by the ductile mode at all applied stresses, while the fracture in He + CH_4 environment occurred by cleavage mode at lower applied stresses and by ductile mode at higher applied stresses. Totemeier et al. [14] have also investigated the creep fatigue behavior of alloy 617 in inert gaseous and air environments at 1000 °C. For most test conditions, the fatigue lives were longer in the inert gaseous environments than in the air environment. Cavitation damage was observed in the tensile hold periods in all environments.

This research investigates the isothermal oxidation, creep behavior, and associated microstructures of the alloy 617 foil specimens at high temperatures in air environment. The oxidation tests were performed at 800, 900 and 1000 °C. The weight gains were measured after the predetermined oxidation hours. The

* Corresponding author. Tel.: +82 62 530 1668; fax: +82 62 530 1689.
E-mail address: kjkang@chonnam.ac.kr (K.J. Kang).

0022-3115/$ - see front matter © 2008 Elsevier B.V. All rights reserved.
doi:10.1016/j.jnucmat.2008.04.021

microstructures of oxides were investigated under scanning electron microscope (SEM) and energy dispersive X-ray (EDX) mapping. The creep tests was performed to evaluate the influences of temperature and applied stresses on the creep rupture life, rupture strain, steady state creep rate, and associated microstructure. The relation between the creep properties and changes in microstructure such as dynamic recrystallization were analyzed through an optical microscope. The creep life, t_f, and total creep strain to failure, ε_f, were measured *in situ*. The steady state creep rates, $\dot{\varepsilon}_{ss}$, and the apparent activation energy, Q_{app}, for the creep deformation were calculated from the strain-time-temperature curves.

2. Experimental protocol

2.1. Materials and preparation

Commercially available alloy 617 was used for the experiments. The elemental composition (wt%) of alloy 617 is given in Table 1. The fabrication of the specimens for oxidation/creep tests is shown in Fig. 1. A sheet of alloy 617 was cut into pieces of thicknesses from 0.50 to 1.00 mm using the wire-cutting technique. These samples were annealed (being enclosed in a vacuum sealed quartz tube) in a tube furnace at 950 °C for 17 h. Thereafter, these samples were cold rolled and cut into ribbons with lateral dimensions ~5 mm × 50 mm. Prior to tests, all the foil specimens were annealed in vacuum again for the above-mentioned time and temperature to promote recrystallization, stabilize the grain structure, and eliminate the residual stress. Surface oxides were then removed by surface-polishing with 1000, 1200, 1500 grit SiC papers. Polishing was also performed with a paste of 1 μm diamond suspension. After each preparation step, the specimens were thoroughly cleaned ultrasonically with acetone and dried by blowing with pure compressed nitrogen gas. The dimensions and weight were measured before and after each experiment within accuracies of ±10 μm and ±10 μg, respectively.

2.2. Micro creep test system

The micro creep test machine and its schematic diagram are shown in Figs. 2 and 3, respectively. The range and the accuracy of the test machine are given in Table 2. A specimen of thin ribbon (polished and ultrasonically cleaned) was mounted between the upper and lower friction grips and surrounded by a quartz tube (20 mm inner diameter) to shield it from turbulence. The 2 mm gaps between the tube and the upper/lower grip induced upward convection of air along the surface [15–16]. The load was controlled to an accuracy of ±100 μN by a mechanical balance (OHAUS 2389) mounted on the top of the test frame. The load path was supported through an air bearing, which also served as a medium for cooling the specimen near the grips. The specimens were Joule heated through stainless steel grips by using a direct current (DC) power supply (HP 6573 A). The displacement of the specimen was measured on the top end of the moving upper grip by an infrared laser position sensor (EM4SYS TBMPH-1). The lower grip was air cooled by attached fins and fans to assure that the load cell (Kyowa LC-5KA) did not get overheated. The temperature was monitored by a pyrometer (CHINO, IR-FA1NNN), which detects infra-red radiation of wavelength, $\lambda \approx 1.55$ μm. Load, temperature, and displacement were monitored *in situ* and controlled by using an A/D, D/A board (Data Translation DT 322) with control software.

Table 1
Elemental composition (wt%) of alloy 617

Element	Ni	Cr	Co	Mo	Al	Fe	Ti	Mn	Si	C
Wt%	Bal	21.6	12.5	9.5	1.2	0.9	0.3	0.1	0.1	0.08

2.3. Creep test and measurement procedure

For calibration of the pyrometer, a thermocouple, which was sandwiched by two foils of the same dimensions and materials, was used and calibrated for up to 72 h at the temperatures of the creep and the oxidation tests. For each creep test, a separate specimen was installed in the test rig. Next, a fixed load, P, was applied, and the creep displacement was measured *in situ*. After the creep fracture, the specimen was removed from the test system. Then, the specimen was mounted with resin and polished up to 1 μm diamond suspension. After polishing, the specimen as etched at room temperature in HCl-15 ml/HNO_3-5 ml solution for 60–90 s. Then, the specimen microstructure near the fracture was observed under an optical microscope.

2.4. Measurement of weight gain and oxide composition

To measure the weight gain due to oxidation, the specimens were removed from the test system after each period of predetermined oxidation hours. Then, the oxidation rate was calculated as the weight gain per unit area as follows:

$$\Delta W/S = (W_t - W_o)/S_o, \quad (1)$$

where W_o is the weight before oxidation, W_t is the weight after oxidation, and S_o is the surface area before oxidation. After the measurement of weight gain, specimens were prepared for the microstructure observation. The specimens were cut normal to the surface and polished with up to 1 μm diamond suspension. The surface/sub-surface oxides and microstructure were observed under the SEM. To obtain the composition of the oxide elements, EDX-mapping was used.

3. Results and discussion

3.1. Oxidation in air

The oxidation tests were conducted on foil specimens at 800–1000 °C in air environment. The specimens were exposed to air for oxidation for up to 82 h. Fig. 4 shows the variation of TGO thicknesses with oxidation time. The TGO thickness increases with oxidation time. The EDX-mapping results of the cross-section after oxidation at 800, 900 and 1000 °C for 48 h are shown in Fig. 5(a)–(c), respectively. In the figures, the red, blue and green spots indicate oxygen, chromium, and aluminum, respectively. The uniform surface oxide scale was identified as chromia (Cr_2O_3), and the discrete internal oxide was alumina (α-Al_2O_3). The surface oxide layer, Cr_2O_3, does not monotonically increase at 1000 °C. Fig. 6(b) shows the EDX-mapping micrograph of the specimen oxidized at 1000 °C for 82 h. Compared with Fig. 5(c), the surface oxide decreases from 12 μm to 7 μm even though the exposure time increases. (Notice that the two micrographs have different scale bars.) The penetration depth of the internal oxide increases from 4 to 30 μm as the oxidation temperature increases from 800 to 1000 °C for 48 h. The larger penetration depth of internal oxidation was caused by the enhanced diffusion rate of oxygen through the oxide scale at higher temperatures. The weight gain curves of alloy 617 for 800–1000 °C in air environment are shown in Fig. 7. The weight gain curves follow a parabolic curve at 800 and 900 °C with oxidation time. The increasing surface oxide thickness and deeper penetration of internal oxidation with respect to time and temperature as shown in the figures would have contributed to the weight gain. However, at 1000 °C, after the initial

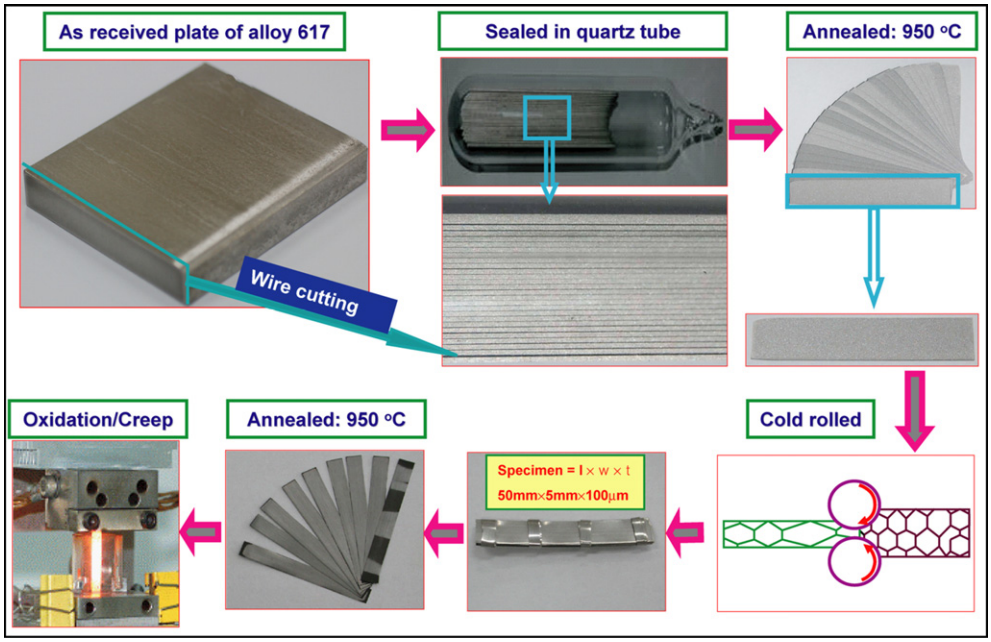

Fig. 1. The preparation process of the foil specimens.

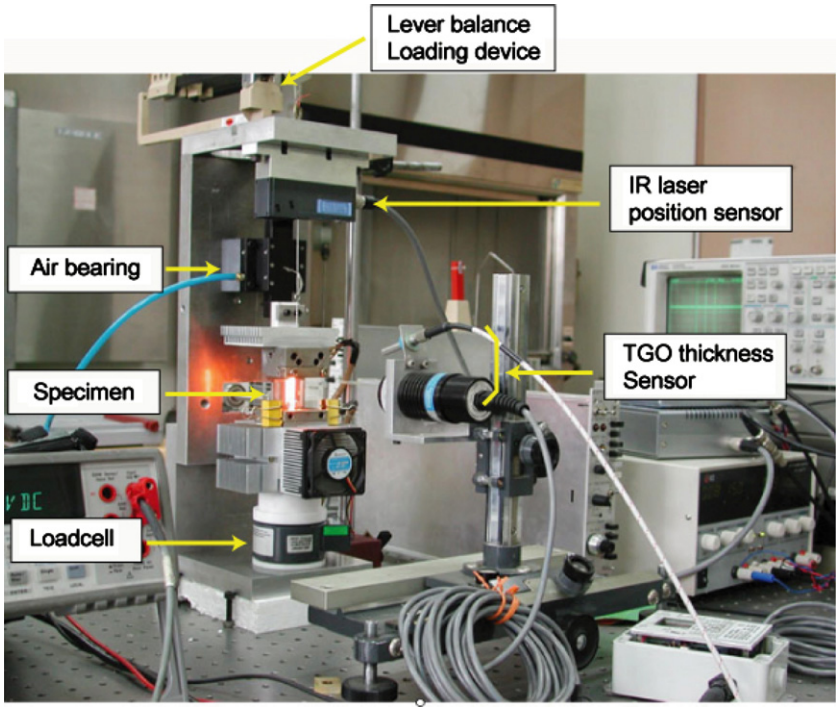

Fig. 2. Micro-creep test system with TGO thickness sensor (front).

weight gain following a parabolic curve, weight loss is observed. The weight loss could have been induced mainly by the spalling and evaporation of the surface oxide Cr_2O_3 from the surface of the specimen that become thermodynamically unstable and begin to evaporation at 1000 °C. The evaporation of Cr_2O_3 occurs according to the following equation [17],

$$Cr_2O_3 + \frac{3}{2}O_2(g) \rightarrow 2CrO_3(g) \quad (2)$$

Other sources of weight loss, like decarburization and thermal etching could also be considered. However, their contribution to weight loss was considered not so significant [18]. The oxidation characteristics of Cr-containing alloy 617, has demonstrated that the wrought alloys usually develop chromium-rich surface dense oxide scales and internal discrete aluminum oxide in 'balanced' VHTR environments [19–21]. But above a critical temperature, T_C, (>950 °C) the oxide scale chromia suffers from a destructive reaction and cannot provide any protection against further corrosion.

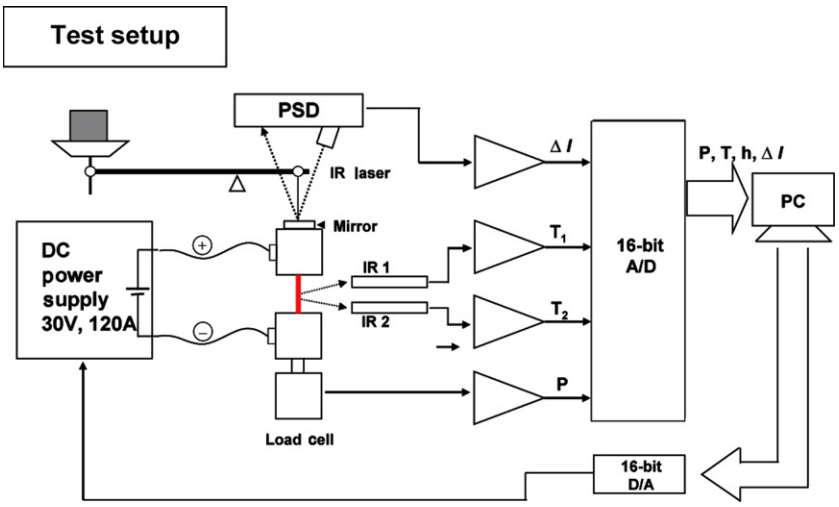

Fig. 3. Schematic diagram of micro-creep tester.

Table 2
Specifications of the micro-creep test system

Properties	Range	Precision
Load	0–50 N	±0.001 N
Displacement	−10 to +10 mm	1 μm
TGO thickness	0–6 μm	0.1 μm
Temperature	RT ~ 1300 °C	3 °C
Specimen size	Length: 40–100 mm, Thickness: 0.05 ~ 1 mm width: 4–10 mm	
Temperature slew rate	50 °C/s	
Minimum period of load cycle	20 s	

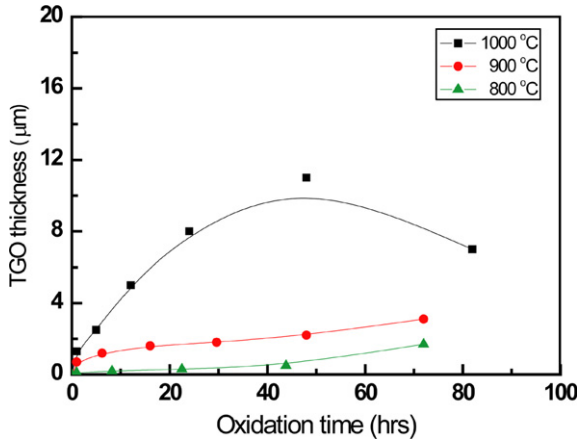

Fig. 4. Variation of TGO thicknesses versus oxidation time at 800, 900 and 1000 °C.

This reaction, called 'microclimate reaction' was especially investigated by Christ et al. [12] on the nickel base alloy 617.

In general, aluminum added to the Ni-base alloy primarily improves the high temperature oxidation resistance because it partitions and stabilizes the surface oxides, for example, Cr_2O_3 [22–23]. However, no evidence of aluminum partitioning into the surface oxide was observed in this study. Instead, aluminum formed discrete internal oxides in the matrix beneath the surface oxide, even though, for the initial stage of oxidation as shown in Fig. 6(a). The EDX mapping revealed that the surface oxide was observed as chromia of 1.3 μm thickness on the surface and internal discrete oxidation was alumina for 1 h oxidation at 1000 °C.

3.2. Uniaxial creep response of rolled and annealed foils

Fig. 8 shows the creep curves of as-rolled and rolled-annealed foil specimens of alloy 617 at 900 °C of applied stress 35 MPa. The creep rupture life increases from ~2 h for the as-rolled specimen to ~39 h for the rolled-annealed specimen. The secondary and tertiary creeps were observed in the as-rolled specimen, and the primary creep as well as the secondary and tertiary creeps was observed in the rolled-annealed specimen. These creep curves indicate the microstructural difference between the as-cold-rolled and the rolled-annealed foil specimens. The cold rolling process deformed the microstructure of alloy 617 at room temperature, resulting in disorders of the crystal structure, an increase in yield strength, and instability at high temperature. The annealing process induced recrystallization in the microstructure. The creep properties were strongly dependent on the recrystallization. The steady state creep rate, $\dot{\varepsilon}_{ss}$, for the as-rolled specimen was $28.7103 \times 10^{-4}\ s^{-1}$, which decreased to $1.2509 \times 10^{-6}\ s^{-1}$ for the rolled-annealed specimen. The elongation, $\Delta l = l_f - l_i$, of the as-rolled specimen was 37.33% and that of the rolled-annealed specimen was 30.45%. The higher creep resistance of the rolled-annealed specimen indicated that the smaller grains, i.e., the denser grain boundaries restrained diffusional flow. The secondary and tertiary creeps took more time in the rolled-annealed specimen at the same temperature and the same applied stress than in the as-rolled specimen. In the following creep tests, we used only annealed foil specimens.

3.3. Uniaxial creep response and associated microstructure

Creep strain versus rupture life curves measured for the foil specimens at 800, 900 and 1000 °C under different applied stresses are shown in Figs. 9–11, respectively. The applied stress levels were 48–120 MPa at 800 °C, 35–60 MPa at 900 °C, and 20–48 MPa at 1000 °C. The effect of applied stress on rupture life at a given temperature is evident from these curves. Fig. 12 shows the creep rupture life, t_r, versus applied stress with temperature. The creep rupture curves show similar behavior at all the temperatures. Fig. 13 shows the variation of rupture strain versus the applied stress at all the three temperatures. The increase in rupture strain with the increase of temperature from 800 to 1000 °C

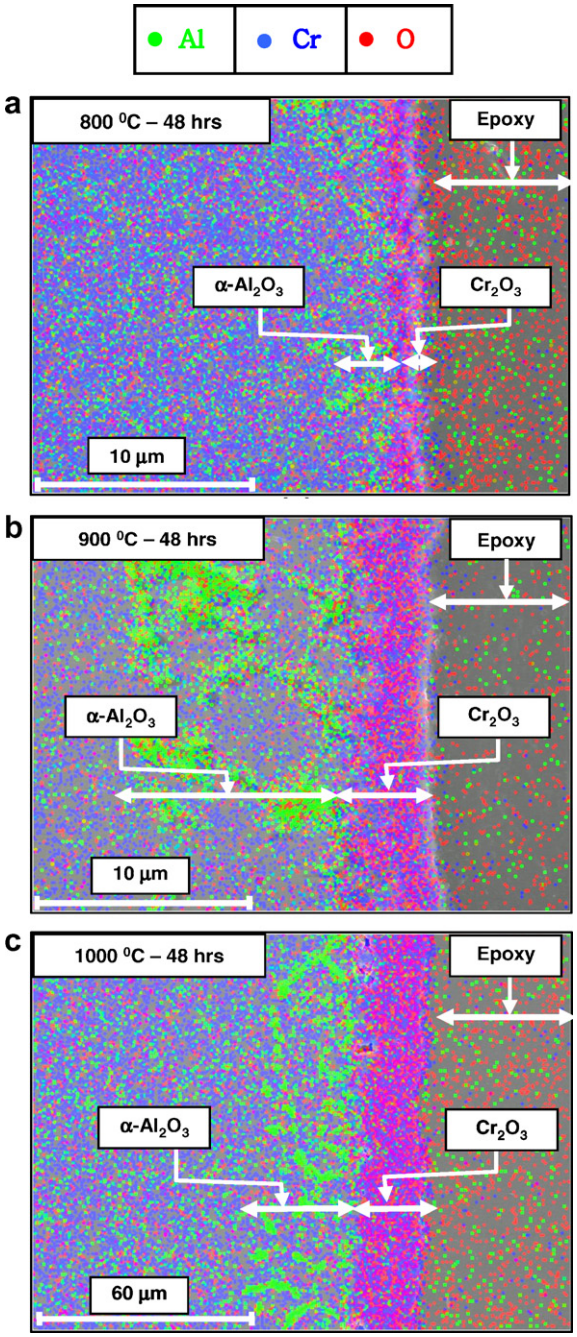

Fig. 5. EDX mapping of cross section of oxidized specimens for 48 h, (a) 800 °C (b) 900 °C and (c) 1000 °C; the oxide layers differentiated by color spots: red spots for oxygen; blue spots for chromium; green spots for aluminium. (For interpretation of the references to colour in this figure legend, the reader is referred to the web version of this article.)

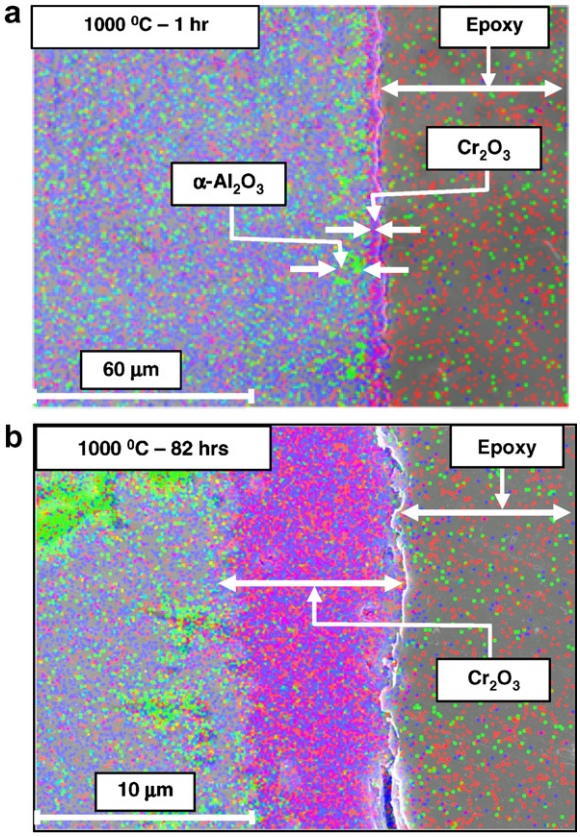

Fig. 6. EDX mapping of cross section of oxidized specimen at 1000 °C for (a) 1 h and (b) 82 h.

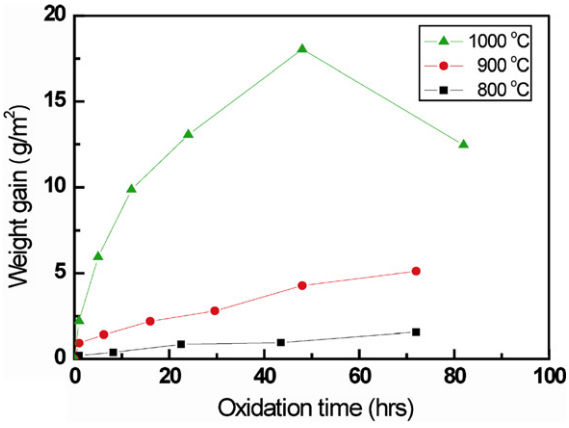

Fig. 7. Weight gain versus oxidation time at 800, 900 and 1000 °C.

indicated more ductile behavior at 1000 °C than at 800 °C, and virtually no direct relevance with the applied stress.

Fig. 9 shows the curves of creep strain versus time measured for 800 °C. In the figure, the primary creep is absent, and only secondary and tertiary creeps are observed in the creep curves as the applied stresses decrease from 120 to 60 MPa, while at the lowest stress, 48 MPa, the primary, secondary and tertiary creeps are observed. For arbitrating the primary creep at higher applied stresses, the initial portions of the creep curves are enlarged in the insert for Figs. 9–11. For the microstructure of creep tested specimens, all the specimens were polished normal to the tensile loading then optical microscopic picture near the fracture region were taken. The optical microscopic pictures of the lowest and highest applied stresses are shown in Fig. 14(a) and (b), respectively. Dynamic recrystallization (DRX) was observed in all the specimens including those with the very short life. It is an effective metallurgical process for grain refinement during hot deformation. At the highest applied stress, the growth grains during DRX were found uniform while at the lowest applied stress were observed the serrated grains. The fine and serrated grains were considered as evidence of dynamic recrystallization. DRX is the strengthening mechanism during hot deformation caused by the generation and migration of high angle boundaries inside the sub-grains [24–25]. The average grain size decreased from 20 to 4 µm as the applied stresses increased from 48 to 120 MPa. Voids were found only at the lowest applied stress

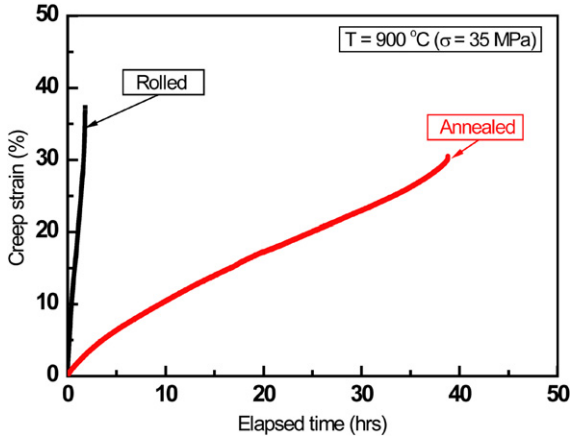

Fig. 8. Curves of creep strain versus time for alloy 617 of as-rolled specimen and rolled-annealed specimen at 900 °C of applied stress 35 MPa.

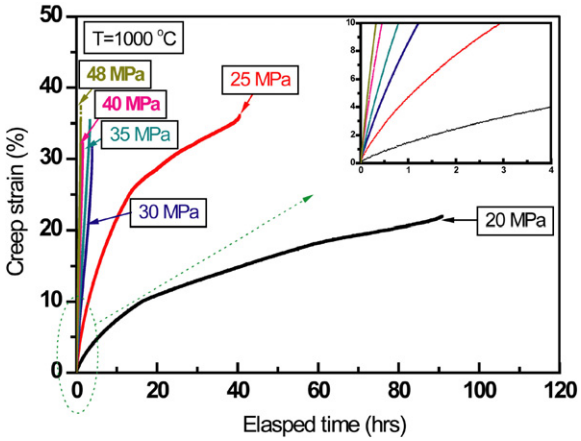

Fig. 11. Curves of creep strain (%) versus time (h) of alloy 617 at 1000 °C in air environment with enlarges of initial strain.

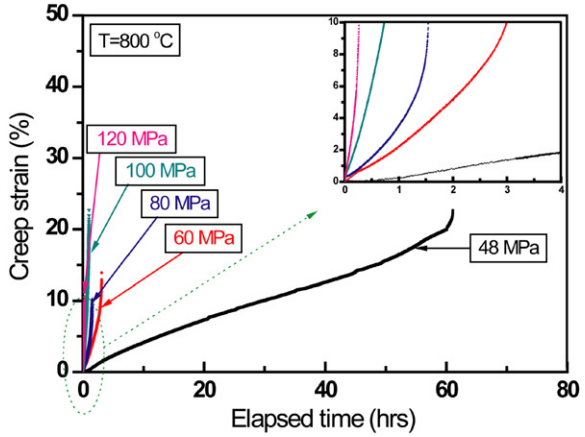

Fig. 9. Curves of creep strain (%) versus time (h) of alloy 617 at 800 °C in air environment with enlarges of initial strain.

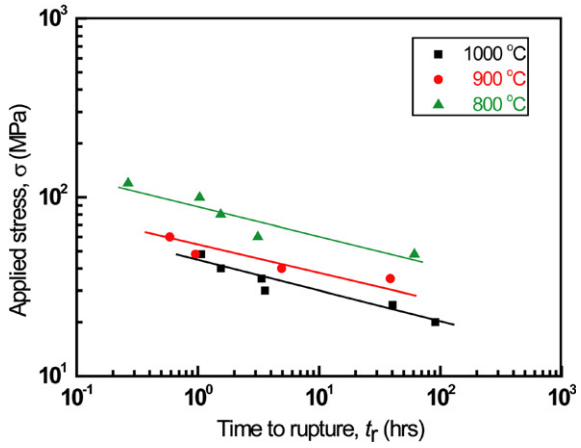

Fig. 12. Creep behavior of alloy 617 in air environment at 800, 900 and 1000 °C.

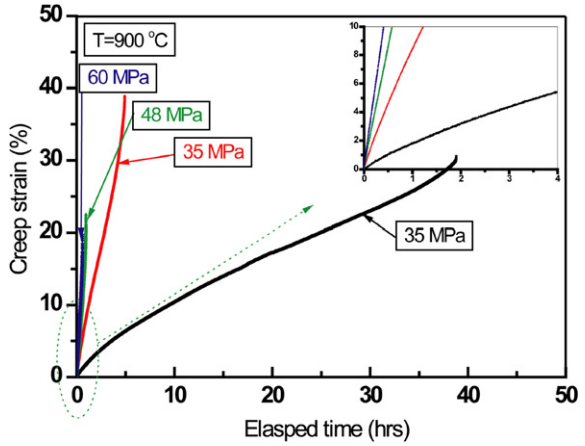

Fig. 10. Curves of creep strain (%) versus time (h) of alloy 617 at 900 °C in air environment with enlarges of initial strain.

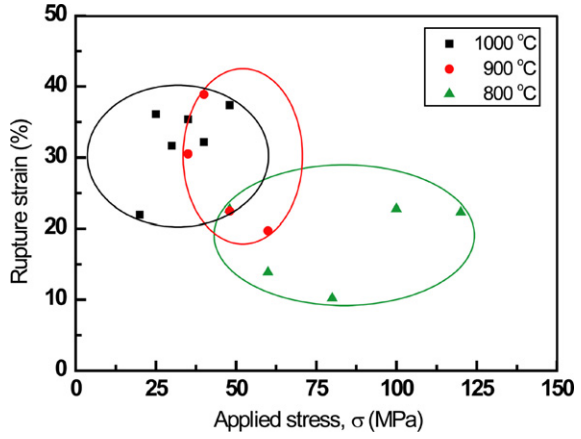

Fig. 13. Variation of rupture strain with applied stress of alloy 617 in air environment at 800, 900 and 1000 °C.

of 48 MPa along the grain boundaries on the surface and also interior near the fracture region as shown in the figure. While many crack like features and cracks were found on the surface in all creep tested specimens near the fracture region. In this case, the void formation in interior of the specimen at the lowest applied stress can be caused by the longest elapsed time or the slow deformation. The TGO formation on the surface was also observed thicker than other higher applied stresses. The thicker TGO indicates more vacancy diffusion. The cavity growth process at grain boundaries at elevated temperature has long been suggested to involve vacancy diffusion. Diffusion occurs by cavity surface migration and

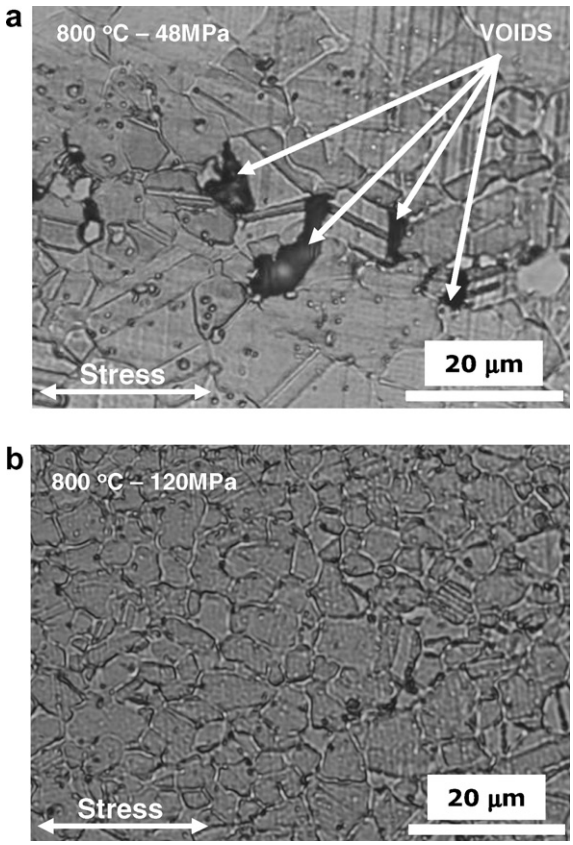

Fig. 14. Microstructure of creep tested specimen of alloy 617 at 800 °C (a) 48 MPa (b) 120 MPa.

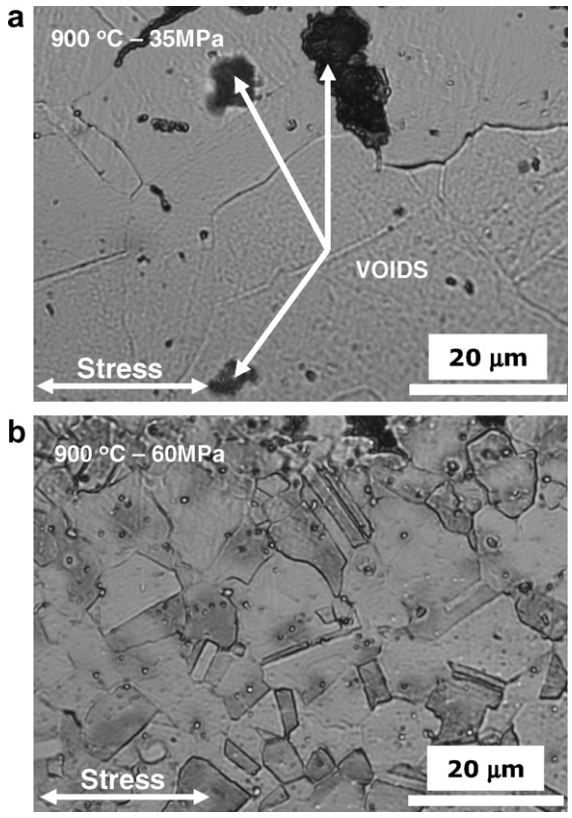

Fig. 15. Microstructure of creep tested specimen of alloy 617 at 900 °C (a) 35 MPa (b) 60 MPa.

subsequent transport along the grain boundary, with either diffusive mechanism having been suggested to be controlling, depending on the specific conditions. This contrasts with creep void growth at lower temperature where cavity growth is accepted to occur by plasticity [26].

Fig. 10 shows the curves of creep strain versus time measured for 900 °C. In the figure, the secondary and tertiary creeps are observed in the creep curves as the applied stresses decrease from 60 to 48 MPa, while at 40 and 35 MPa, the primary, secondary and tertiary creeps are observed. The optical microscopic pictures taken after the creep test near the fracture region for the lowest and highest applied stresses at 900 °C are shown in Fig. 15(a) and (b), respectively. Dynamic recrystallization was also observed. These figures clearly indicate that the average grain size decreased from 50 to 10 μm as the applied stresses increased from 35 to 60 MPa. Voids were also observed at the lowest applied stress of 35 MPa along the grain boundaries.

Fig. 11 shows the curves of creep strain versus time measured for 1000 °C. In the figure, the primary, secondary and tertiary creeps are observed in all the creep curves as the applied stresses decrease from 48 to 20 MPa. The optical microscopic pictures taken after the creep test near the fracture region for the lowest and highest applied stresses are shown in Fig. 16(a) and (b), respectively. In this case, only partial dynamic recrystallization was observed, and the average grain size was found to be ~15–50 μm at all the applied stresses. The grain boundary cavities and the elongation of grains were observed in all the creep tested specimens.

From the analysis of the microstructure, no voids were found inside the creep tested specimens at 800 and 900 °C, except at the lowest applied stresses near the fracture region. At 1000 °C, however, the voids were always found along the grain boundaries. The recrystallization, which induced microstructural changes such as the coarsening of the carbide and the formation of new grains, degraded the strength. The presence or absence of carburization/decarburization in our test specimens in air environment could not be determined.

Fig. 17 shows the curves of the time-to-1% strain versus applied stress of alloy 617. The open symbols of triangles, circles and squares, respectively, represent those measured at 800, 900 and 1000 °C in this work. There are two other sets of data in comparison. One set is from the authors' coworkers, which is marked the star symbols with 'KAIST' and the other is from an old reference, which is marked by the solid symbols with 'ORNL' [27]. The authors and coworkers shared an identical raw material of Alloy 617. Only difference was in the fabrication and heat treatment. The specimens in this work had been heavily rolled into a shape of foil, and annealed for 17 h at 950 °C and furnace-cooled. Contrarily, the coworkers used the raw material as received when they prepared the typical cylindrical specimens. If the difference in the fabrication and heat treatment is considered, the data from this work and those marked the star symbols can be regarded to agree fairly well despite of the difference in the size. The difference from the data marked the solid symbols with 'ORNL' is significant. One possible reason is difference in the heat treatment. They annealed the specimens at the much higher temperature 1177 °C and quenched. According to the author's work on annealing temperature effect on creep strength [28], the lower annealing temperature results in the shorter creep life. There might be difference in the material itself.

3.4. Temperature and stress dependence of creep

The steady state creep rate, $\dot{\varepsilon}_{ss}$, in crystalline materials involves a thermally activated process [29–31],

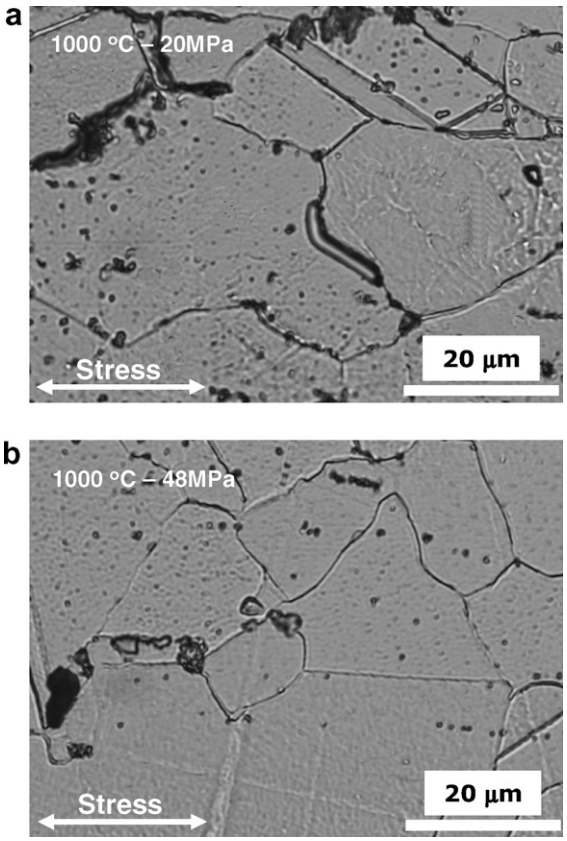

Fig. 16. Microstructure of creep tested specimen of alloy 617 at 1000 °C (a) 20 MPa (b) 48 MPa.

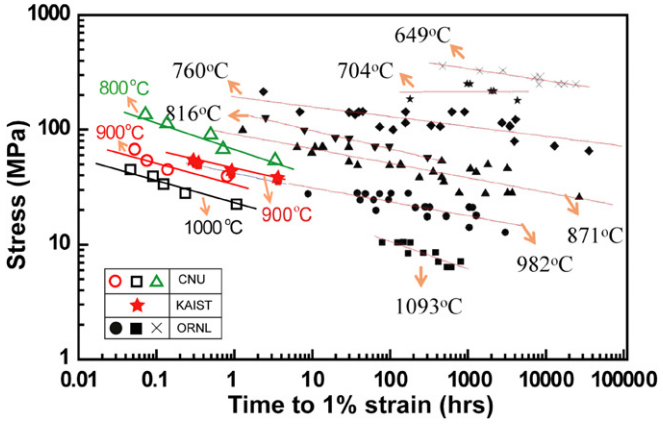

Fig. 17. Creep data of the foil specimens compared with those of bulk specimens [21], time to 1% strain (h) versus applied stress of alloy 617 at 800, 900 and 1000 °C.

$$\dot{\varepsilon}_{ss} = A\sigma^{n} \exp\left[-\frac{Q_{app}}{RT}\right] \quad (3)$$

where σ is the applied stress, n is the stress exponent, Q_{app} is the apparent activation energy for creep mechanism, A is a constant, $R \sim 8.368\ \mathrm{JK^{-1}mol^{-1}}$ is the universal gas constant and T is the absolute temperature. Creep rates were calculated from the slope of the steady state region of the creep strain versus rupture life curves shown in Figs. 9–11. Fig. 18 shows variation of the steady state creep rates with applied stresses at 800, 900 and 1000 °C. The steady state creep rate, $\dot{\varepsilon}_{ss}$, decreases from $3.9637 \times 10^{-5}\ \mathrm{s^{-1}}$ to $4.7240 \times 10^{-7}\ \mathrm{s^{-1}}$ as the applied stresses decrease from 120 to 48 MPa at 800 °C and from $4.4575 \times 10^{-5}\ \mathrm{s^{-1}}$ to $1.1250 \times 10^{-6}\ \mathrm{s^{-1}}$ as the applied stresses decrease from 60 to 35 MPa at 900 °C, while at 1000 °C, $\dot{\varepsilon}_{ss}$, decrease from $4.9251 \times 10^{-5}\ \mathrm{s^{-1}}$ to $1.18788 \times 10^{-6}\ \mathrm{s^{-1}}$ as the applied stresses decrease from 48 to 20 MPa.

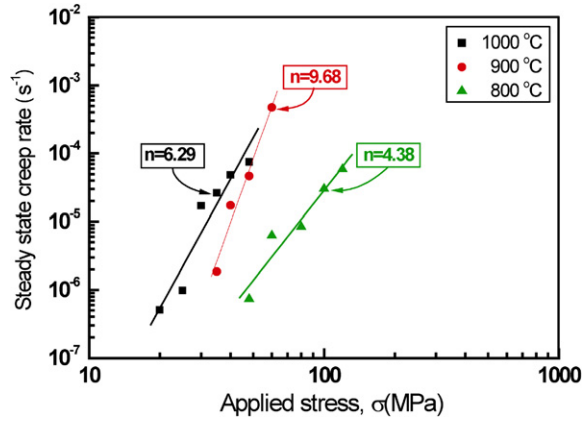

Fig. 18. Stress dependence of steady state creep rate of alloy 617 at 800, 900 and 1000 °C in air environment. Values of apparent stress exponent, n are also shown in the figure.

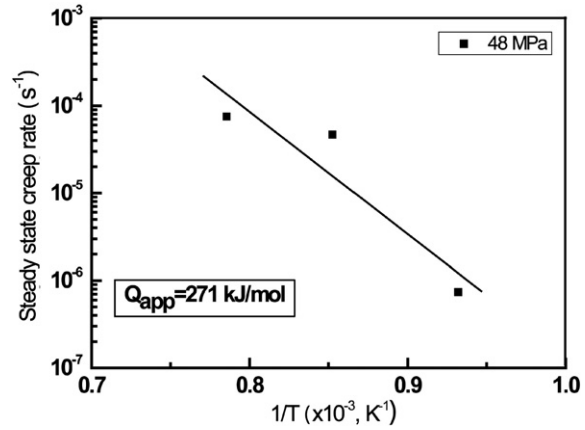

Fig. 19. The temperature dependence of steady state creep rate on applied stress of 48 MPa. The value of the activation energy, Q_{app}, for the creep mechanism is also indicated.

The value of n increases from 4.38 to 9.68 as the temperature increases from 800 to 900 °C and then decreases to 6.29 as the temperature increases to 1000 °C. The temperature dependence of the steady state creep rates, $\dot{\varepsilon}_{ss}$, of alloy 617 is plotted in Fig. 19. For a constant applied stress of 48 MPa, the value of Q_{app} = 271 kJ/mol was calculated by using the $\dot{\varepsilon}_{ss}$ data at 800, 900 and 1000 °C. This apparent activation energy was found to be very close to that observed, 270 kJ/mol, for bulk specimens tested in He + O_2 environment [10].

4. Conclusions

Generally, alloy 617 exhibited parabolic oxidation behavior and the oxidation rate increased with temperature. The surface oxide layer was found to be Cr_2O_3, while the discrete internal oxides beneath the surface oxide were α-Al_2O_3. After the initial weight gain at 1000 °C, the surface oxides became unstable, and weight loss

due to the spallation and evaporation of the surface oxides was observed.

Micro creep tests revealed that the mechanical characteristics of the foil specimens were somewhat different from those of the bulk specimens. Secondary and tertiary creeps were observed at the lowest temperature while primary, secondary and tertiary creeps at the higher temperatures. Dynamic recrystallizations were observed at 800 and 900 °C, while partial dynamic recrystallization at 1000 °C. Grain boundary cavitation and cracks were observed at the lowest applied stresses at 800 and 900 °C, while they were observed at all the applied stresses at 1000 °C. The recrystallization and grain boundary migration compensated the stress concentration caused by straining near the grain boundaries and improved the ductility. We also observed a strong correlation between the average grain size and the applied stress at 800 °C and 900 °C. Times-to-1% strains for the foil specimens were shorter than those for the bulk specimens. The apparent stress exponent, n, varied from 4.38 to 9.68. The apparent activation energy, Q_{app}, was found to be 271 kJ/mol for the foil specimens in air environment, which was very close to 270 kJ/mol observed for the bulk specimens in $He + O_2$ environment.

Acknowledgements

This work was supported by the Basic Atomic Energy Research Institute (BAERI: 2007-01634), which is a part of the Nuclear R&D Programs of the Ministry of Science & Technology (MOST), and one of the authors, S. K. Sharma, was financially supported by BK-21, Republic of Korea.

References

[1] D.J. Lee, D.J. Kim, C.H. Jang, in: Proceedings of ICAPP, Nice, France, May 2007, p. 419.
[2] T. Angeliu, J. Ward, J. Witter, Assessing the effects of radiation damage on ni-base alloys for the prometheus space reactor system, LM-06K033, P.O. Box 1072, Schnecetady, New York, USA, April 2006.
[3] F.M. Olbersleben, N. Kasik, B. Ilschner, F.R. Aria, Mater. Mat. Trans. A 30 (1999) 981.
[4] <www.specialmetals.com>.
[5] A. Kewther, B.S. Yilbas, M.S.J. Hashmi, J. Mater. Eng. Perform. 10 (2001) 108.
[6] M.A. Kewther, B.S. Yilbas, M.S.J. Hashmi, Indust. Lub. Tribol. 53 (2001) 112.
[7] M.K. Ali, M.S.J. Hashmi, B.S. Yilbas, J. Mater. Proc. Tech. 118 (2001) 45.
[8] D. Allen, J.P. Keustermans, S. Gijbels, V. Bicego, Mater. High Temp. 21 (2004) 55.
[9] L. Tan, K. Sridharan, T.R. Allen, J. Nucl. Mater. 371 (2007) 171.
[10] P.S. Shankar, K. Natesan, J. Nucl. Mater. 366 (2007) 28.
[11] L. Huang, X.F. Sun, H.R. Guan, Z.Q. Hu, Oxid. Met. 65 (2006) 391.
[12] H.J. Christ, U. Kunecke, K. Meyer, HG. Sockel, Mater. Sci. Eng. 87 (1987) 161.
[13] M. Tamura, H. Esaka, K. Shinozuka, ISIJ Int. 39 (1999) 380.
[14] T.C. Totemeier, H. Tian, Mater. Sci. Eng. A 468–470 (2007) 81.
[15] S.S. Lee, S.K. Sun, K.J. Kang, Oxid. Met. 63 (2005) 73.
[16] K.J. Kang, C. Mercer, Mater. Sci. Engg. A 478 (2008) 154.
[17] N. Birks, G.H. Meier, F.S. Pettit, Introduction to the High temperature Oxidation of Metals, Second ed., Cambridge University, Cambridge, UK, 2006 (Chapter 4).
[18] C.H. Jang, D.J. Lee, D.J. Kim, Int. J. Pres. Ves. Pip. 85 (2008) 368.
[19] T. Hirano, M. Okada, H. Araki, T. Noda, H. Yoshida, R. Watanabe, Metall. Trans. A 12 (1981) 451.
[20] R.N. Wright, Summary of Studies of Aging and Environment effect on Inconel 617 and Hayans 230, Idaho National Laboratory, INL/EXT-0611750, 2006.
[21] F. Rouillard, C. Cabet, K. Wolski, A. Terlain, M. Tabarant, M. Pijolat, F. Valdivieso, J. Nucl. Mater. 362 (2007) 248.
[22] J. Huang, Oxid. Met. 53 (2000) 273.
[23] R.H. Hook, Nucl. Tech. 66 (1984) 283.
[24] E. Brunger, X. Wang, G. Gottstein, Scripta Mater. 38 (1998) 1843.
[25] X. Wang, E. Brunger, X. Wang, G. Gottstein, Mater. Sci. Eng. A 290 (2000) 180.
[26] M.E. Kassner, T.A. Hayes, Int. J. Plast. 19 (2003) 1715.
[27] C.H. Jang, D.J. Lee, D.J. Kim, International Workshop on Creep-Fatigue Design and Assessment, Korea University, Seoul, Korea, October 2006.
[28] S.K. Sharma, F.X. Li, K.J. Kang, Mater. Charact. (2008), submitted for publication.
[29] J.S. Huo, J.T. Gou, L.J. Zhou, X.Z. Qin, G.S. Li, J. Mater. Eng. Perform. 16 (2007) 55.
[30] T.C. Totemeier, T.M. Lillo, Metall. Mater. Trans. A 36 (2005) 785.
[31] N.E. Dowling, Mechanical Behavior of Materials, 2nd Ed., Prentice Hall, New Jersey, USA, 1999.